J. Mech. Phys. Solids 155 (2021) 104545

Contents lists available at ScienceDirect

Journal of the Mechanics and Physics of Solids

journal homepage: www.elsevier.com/locate/jmps

Probing the buckling of pressurized spherical shells

Arefeh Abbasi, Dong Yan, Pedro M. Reis *

Flexible Structures Laboratory, Institute of Mechanical Engineering, École Polytechnique Fédérale de Lausanne, 1015 Lausanne, Switzerland

ARTICLE INFO

Keywords:
Spherical shells
Buckling
Imperfection sensitivity
Indentation

ABSTRACT

The prediction of the critical buckling conditions of shell structures is plagued by imperfection sensitivity. Non-destructive testing through point-load probing has been recently proposed to map the stability landscape of cylindrical shells. However, the counterpart procedure for spherical shells is still debatable. Here, we focus on the mechanical response of pressurized spherical shells containing a single dimple–like defect to a point probe. Combining experiments, finite element modeling, and existing results from classic shell theory, we characterize the nonlinear force-indentation response of imperfect shells at different pressurization levels. From these curves, we seek to identify the critical buckling pressure of the shell. In particular, the indentation angle is varied systematically to examine its effect on the probing efficacy. We find that the critical buckling point can be inferred non-destructively by tracking the maxima of the indentation force–displacement curves, if the probe is implemented sufficiently close to the defect. When probing further away from the defect, the test fails in predicting the onset of buckling since the deformation due to indentation remains localized in the vicinity of the probe. Using FEM simulations and shallow shell theory, we quantify the characteristic length associated with this localized deformation, both in the linear and nonlinear regimes. Our results demonstrate the limiting conditions of applicability for the usage of probing as a non-destructive technique to assess the stability of spherical shells.

1. Introduction

The buckling of thin shells has long been a research subject in the structural mechanics community (Babcock, 1983; Samuelson and Eggwertz, 1992; Elishakoff, 2014). The prediction of critical loads is at the basis of the design stage of shell structures across length-scales, from microscopic capsules to large-scale fuel tanks (Datta et al., 2014; Pedersen and Jensen, 1995). For a spherical shell, one of the most commonly used geometries in engineering shells, the critical load under a uniform pressure loading was first proposed by Zoelly (1915) in 1915, based on a linear buckling analysis,

$$p_c = \frac{2E}{\sqrt{3(1-\nu^2)}}\left(\frac{h}{R}\right)^2, \tag{1}$$

where R and h are radius and thickness of the shell, respectively, and E and ν are Young's modulus and Poisson's ratio of the material. Notwithstanding, subsequent studies (Tsien, 1942; Kaplan and Fung, 1954; Homewood et al., 1961; Seaman, 1962; Krenzke and Kiernan, 1963; Carlson et al., 1967) indicated that this prediction, p_c, was in systematic disagreement with experimental measures of the buckling pressure, p_{max}, consistently yielding overestimates. The ratio between p_{max} and p_c is classically referred to as the *knockdown factor*, $\kappa_d = p_{max}/p_c$, which can be as low as 0.2 (Lee et al., 2016b). This discrepancy between theory and experiment is

* Corresponding author.
E-mail addresses: arefeh.abbasi@epfl.ch (A. Abbasi), dong.yan@epfl.ch (D. Yan), pedro.reis@epfl.ch (P.M. Reis).

https://doi.org/10.1016/j.jmps.2021.104545
Received 7 January 2021; Received in revised form 7 May 2021; Accepted 15 June 2021
Available online 21 June 2021

attributed to the high imperfection sensitivity of shells, meaning that the load at which a shell buckles depends strongly on defects in the geometry and material heterogeneity of the shell (in reverse, $\kappa_d = 1$ for a perfect spherical shell). These imperfections can be imparted onto a shell during fabrication or operational usage.

Early attempts to rationalize the origin of knockdown factors were mostly unsuccessful (von Kármán and Tsien, 1939; Karman, 1940, 1941; Tsien, 1942). In 1945, Koiter (1945) carried out a breakthrough theoretical work by developing a general theory of stability for elastic systems subject to conservative loading. Following this seminal development, a vast series of studies were subsequently preformed to study the fundamental basis of imperfection sensitivity, identifying defects (*e.g.*, in geometry (Hutchinson et al., 1971; Budiansky and Hutchinson, 1972), loading (Bijlaard and Gallagher, 1960), or boundary conditions (Kobayashi, 1968)) as the culprits of the knockdown, $\kappa_d < 1$. Despite the extensive theoretical and computational studies since Koiter, practical knowledge on shell buckling has remained primarily qualitative, with a striking difficulty to map the characterization of the imperfections of a realistic shell into concrete prediction for its buckling load. Consequently, for decades, engineers have been relying primarily on acquired experience, *ad hoc* guidelines, and over-conservative engineering codes (Hilburger, 2012). Given the undeniable importance of the design of engineering shell structures against buckling, which can lead to the global failure, the field begs for comprehensive, systematic, and generalizable tools, rooted in a predictive mechanics-based framework, that can accurately capture knockdown factors.

It has become evident that the gap in understanding between theory and practice has been mostly due to a misalignment in the type, quality and volume of experimental data that is available to provide the necessary physical insight required to construct appropriate models. Indeed, experimental research on shell buckling has long lagged behind theory and computation (Chen, 1959; Babcock, 1983; Seaman, 1962; Hutchinson et al., 1971). Recently, to fill this gap, Lee et al. (2016a) have revived the experimental research in shell buckling by introducing a robust, versatile, and precise coating technique to rapid-prototype thin spherical shells in a laboratory setting. This technique can also be modified to produce a precisely engineered defect of controllable geometry in the shell (Lee et al., 2016b; Marthelot et al., 2017; Lee et al., 2019; Yan et al., 2021). For the first time, quantitative relationships were obtained between the critical pressure and the geometry of an imperfection. These experimental advances have played an essential role in the revival of the interest on the buckling of both perfect and imperfect shells (Hutchinson, 2016; Hutchinson and Thompson, 2017a,b, 2018; López Jiménez et al., 2017). However, detailed prior knowledge of the imperfections is still necessary for theoretical or numerical tools to predict the stability.

Toward developing a general framework to characterize the stability of shells, a novel non-destructive probing technique has been proposed and successfully applied to axially compressed cylindrical shells (Thompson, 2015; Thompson and Sieber, 2016; Thompson et al., 2017; Virot et al., 2017). The basis of this approach is to measure the nonlinear response of the shell to a point probe. The force–displacement relationship measured by systematically varying the level of axial compression is used to construct the stability landscape. The area under load–displacement curves gives the energy barrier that must be overcome by any static or dynamic lateral disturbance to trigger the buckling (Thompson, 2015; Thompson and Sieber, 2016; Baumgarten and Kierfeld, 2019). Virot et al. (2017) built an experimental setup to exert a point probe on cylindrical shells under axial compression. The authors provided experimental evidence that the hyper–dimensional landscape fully characterizes the stability of perfect and imperfect cylindrical shells. The complex stability of shells was reduced to a three dimensional phase space description that can be analyzed using modern tools from nonlinear dynamics and dynamical systems. By tracking the ridges of force–displacement curves, the knockdown factor of cylindrical shells could be extrapolated correctly. Recently, Abramian et al. (2020) applied this probing technique to commercial cylindrical shells containing a hole and showed that when the location where buckling nucleates is known, the buckling load of each individual shell can be accurately predicted. Additionally, a new numerical solution was recently proposed, where instead of considering the linear instability of a shell with defects, a finite, nonlinear destabilizing perturbation was imposed on an otherwise perfect shell (Kreilos and Schneider, 2017). In this study, the elastic response of the shell was captured by the Donnell–Mushtari–Vlasov (DMV) theory. The fully nonlinear equilibrium states on the boundary of the unbuckled state's basin of attraction for an axially loaded cylindrical shell were identified. It was shown that, for changes in the applied compression, a single dimple undergoes homoclinic snaking in the circumferential direction until the circumference is completely filled with a ring of buckles.

In a series of related studies, the non-destructive probing technique was recently applied to cylindrical thin shells containing local dimple–like imperfections, both computationally (Fan, 2019; Yadav and Gerasimidis, 2020) and experimentally (Yadav et al., 2021). The proposed algorithm based on the probe force–displacement curves was validated on perfect, as well as imperfect, axially loaded cylindrical shells. More importantly, the influence from background imperfections and the location of probing relative to the imperfections were considered to examine the robustness of the technique. The results showed that the probe has to be set close enough to the dominant defect in the shell to ensure a high–fidelity prediction.

To date, it has remained inconclusive whether the probing technique can serve as an effective way for assessing the stability of spherical shells in a way that parallels the successful case of cylindrical shells mentioned above. The response of perfect spherical shells subjected to external uniform pressure with and without a probe force was recently investigated by Hutchinson and Thompson (2017a,b) based on a small-strain and moderate-rotation shell theory formulation, both under prescribed pressure and prescribed volume change. Thompson et al. (2017) addressed the testing of compressed shell structures using the concept of probing by a controlled lateral displacement to gain quantitative insight into their buckling behavior and to measure the energy barrier against buckling, providing design information about a structure's stiffness and robustness against buckling in terms of energy and force landscapes. The first experimental study on probing of imperfect spherical shells was carried out by Marthelot et al. (2017). They investigated the buckling strength and energy barrier of shells containing a geometric defect, subjected to a simultaneous combination of pressure loading and a probe force. They showed that probing strategy applied on the defect is a successful way to assess the stability of spherical shells. However, by considering a point load located off-axis from the defect, it was found that, the

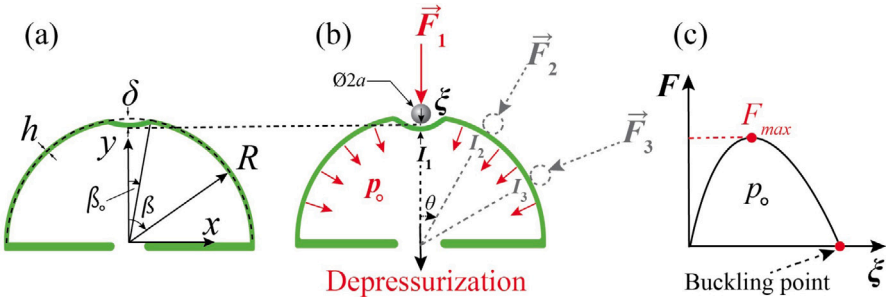

Fig. 1. Definition of the problem. (a) A spherical shell of radius, R, and thickness, h, contains a dimple–like geometric defect at the north pole. The geometry of the defect is characterized by its amplitude, δ, and half-angular width, $\beta_\circ$. (b) The shell is simultaneously depressurized to a preset pressure level $p_\circ$ and then indented radially by a circular rigid indenter of radius a inducing a deflection ξ at the contact point I. The action line of the force, F, is set at an angle θ with respect to the (vertical) axis of symmetry of the defect. To change the probe angle, the indentation is applied at different locations (I_1, I_2, I_3,...). (c) Sketch of a typical probe force versus displacement curve, $F(\xi)$, at the constant preset pressure level of $p_\circ$.

energy barrier measured from the probe is similar to that of a perfect shell, but dramatically jumps down to zero when buckling occurres. However, these experiments were only conducted in limiting cases; the probe was either located exactly at the center of the defect or far away from the defect. Therefore, there is a need to more systematically explore the response of a spherical shell loaded by a probe located in between the two extreme locations. This timely data would indicate the limitations and range of applicability of the probing technique in the context of identifying the critical buckling conditions and encoding the characteristics of the stability of spherical shells.

Here, we have performed a thorough investigation on how the response of an imperfect spherical shell is affected by the location (angle) of indentation with respect to the location of the defect. By analyzing the indentation force–displacement curves measured by a probe positioned at different locations, which are systematically varied, we seek to estimate the critical point and contrast this value with the direct measurement obtained from buckling test. Using shell theory and experimentally validated finite element modeling (FEM), we then describe how the localized nature of indentation of spherical shells dominates the performance of probing and obstructs its usage as a non-destructive technique to predict the buckling conditions of spherical shells.

Our paper is organized as follows. First, we define the problem at hand in Section 2. In Section 3, we describe the experimental methodology to fabricate imperfect shells containing a precisely engineered defect, as well as the experimental protocol followed in the probing tests. Details on the FEM simulations are provided in Section 4. In Section 5.1, we report on experiments and numerical simulations to investigate the response of the fabricated imperfect shell under pressure loading, while simultaneously indenting it at the center of the defect. Then, in Section 5.2 we vary the indentation angle by incrementally moving the indentation point away from the defect to study its influence on the performance of the probe and to examine the applicability of this technique in predicting the knockdown factor of the shell non-destructively. The FEM is validated by comparing numerical predictions to experimental measurements. In Section 5.3, we investigate the localized deformation of pressurized spherical shells under indentation at different locations. Finally, in Section 5.4, we use classic shallow shell theory and the validated FEM to rationalize our results. Specifically, we analyze the localized nature of the indentation and characterize the length scale associated with the indentation neighborhood.

2. Definition of the problem

We consider a thin, elastic, hemispherical shell of radius, R, and constant thickness, h, containing a geometric defect at its north pole; see the schematic diagram in Fig. 1a. As a representative example of a thin shell, in both experiments and simulations, we will focus on a value of the radius-to-thickness ratio of $R/h = 78$, unless otherwise stated (specifically in Section 5.4 where we systematically vary h, and hence, also R/h). The shell is clamped at its equator. The amplitude of the defect, δ, corresponds to the maximum radial deviation of the shell from a perfect hemisphere. Defining β as the polar angle measured from the north pole (where $\beta = 0$), the axisymmetric dimple-like defect extends over the region $0 \le \beta \le \beta_\circ$, with $\beta_\circ$ being its half angular width (*i.e.*, the angular amplitude).

The shell is first loaded under uniform pressure, which is set at a prescribed value, $p_\circ$. The shell is then indented by a point load applied on its outer surface, along its radial direction, while imposing the indentation displacement, ξ. This indentation is performed by a rigid circular indenter of radius a (see schematic in Fig. 1b). The resulting reaction force of the indenter is referred to as the probe force, F. Each indentation test is performed at different pressure levels ($p_\circ$) to obtain the corresponding probe force–displacement curves, $F(\xi)$.

In Fig. 1c, we show a sketch of a representative $F(\xi)$ curve, at a set pressure level (the actual data will be presented in Fig. 4). The probe force first increases with probe displacement to a maximum value ($F_{\max}$), after which F decreases and eventually reaches zero when the shell collapses. If the prescribed pressure is increased to a level such that $F_{\max} = 0$, the shell is loaded at the critical point and the corresponding pressure is the critical load. From the $F(\xi)$ curves measured before reaching the collapse at $F_{\max} = 0$, and motivated by recent work on cylindrical shells (Virot et al., 2017; Hutchinson and Thompson, 2017b; Thompson, 2015; Thompson and Sieber, 2016; Thompson et al., 2017), one may expect that extrapolating the $F_{\max}(p_\circ)$ curve to zero would provide access to

the critical buckling pressure of our spherical shells in a non-destructive manner. We also seek to examine the robustness of this non-destructive technique in testing imperfect spherical shells. Specifically, we focus on the effect of positioning the probe with respect to the location of the defect. To do so, we will systematically vary the angle, θ, between the line of action of the probe force and the axis of symmetry of the defect. We will analyze the nonlinear force–displacement response of indentation exerted at different positions, in order to attest its ability to predict the critical point without a prior knowledge on defect distribution.

3. Experimental methods

In this section, we first present the rapid prototyping technique that we used to fabricate shell specimens containing a precisely engineered imperfection. We then characterize the geometry of defects using optical profilometry. Finally, we detail the apparatus and the experimental protocol that was developed to exert indentation on pressurized imperfect shells.

3.1. Fabrication of the imperfect shell specimens

We fabricated imperfect hemispherical shells containing a precisely engineered geometric defect following the experimental protocol proposed in our recent work (Yan et al., 2021), which itself was built upon a previously developed coating technique (Lee et al., 2016a,b). Next, for completeness, we summarize the basis of the fabrication protocol.

First, we manufactured an elastic mold as the negative of a rigid hemisphere (stainless steel ball, radius 25.4 mm, TIS-GmbH, Germany) using a silicone-based vinylpolysiloxane (VPS) polymer (Elite Double 32, Zhermack, Italy). The mold contained a circular thin region of half angular width 10 ° and thickness 0.5 mm at the pole (Yan et al., 2021). The shell specimen was then fabricated by coating the concave inner surface of the mold with the VPS solution (Fig. 2a1 and a2). The polymer mixture was prepared and poured into the mold by waiting a set time $t_w = 210$ s upon preparation, thereby raising the viscosity (Lee et al., 2016a) to target the desired value of the shell thickness ($h = 327$ μm). To produce a geometric defect in the shell before the polymer was cured, we depressurized the mold to a set pressure level $q = 1.2$ kPa by air extraction (Fig. 2a2). Under this depressurization, the plate–like thin region of the mold deformed inwards and the associated deflections eventually produced the dimple–like geometric defect upon curing. Finally, the thin, elastic, imperfect shell was peeled off from the mold (Fig. 2a3). Using this technique, we were able to vary the geometry of the defect on demand, namely its amplitude δ and half angular width $\beta_\circ$, by setting the applied pressure and the width of the thin region of the mold, respectively. Additional details of the protocol can be found in Ref. Yan et al. (2021).

3.2. Characterization of the shell geometry

Following the protocol presented above, we fabricated shell specimens of radius $R = 25.4$ mm and thickness $h = 327 \pm 11$ μm, yielding a radius-to-thickness ratio of $R/h = 78$. As stated in Section 2, we will fix this value of R/h throughout the manuscript as representative of a thin shell, except for Section 5.4, where h, and hence R/h, will be varied systematically. Borrowing a procedure developed in our previous study (Yan et al., 2021), we characterized the geometry of the fabricated defect through profilometry. The defect profile is represented by the radial deviation of the outer surface of the shell with respect to a perfect sphere, w_I, which was averaged latitude-wise due to axisymmetry. In Fig. 2b, we present a typical example of a defect profile of the shell specimen that will be used in the subsequent indentation tests.

The defect geometry can be described analytically, on the basis of the deformation of the elastic mold during shell fabrication (Yan et al., 2021). The idea is to simplify the thin circular region of the mold as a flat plate clamped at its boundary and describe its deflection under uniform pressure loading by Kirchhoff–Love plate theory (Timoshenko and Woinowsky-Krieger, 1959), suggesting that the profile of the dimple-like defect ($\beta \leq \beta_\circ$), which originates from the deformation of the plate-like region in the mold, can then be written as

$$\frac{w_I(\beta)}{h} = \frac{\delta}{h}\left(1 - \frac{\beta^2}{\beta_\circ^2}\right)^2, \tag{2}$$

where w_I is the out-of-plane displacement of the plate. We note that this description is only valid in the region of the defect. Away from the defect, the shell is spherical: $w_I(\beta)/h = 0$ for $\beta > \beta_\circ$. We have fitted Eq. (2) to the experimentally measured profile, taking the amplitude, δ, and half angular width, $\beta_\circ$, of the defect as fitting parameters, finding excellent agreement between the two (see Fig. 2b). For the particular defect taken as a representative example, we obtained $\overline{\delta} = \delta/h = 0.4 \pm 0.02$ and $\beta_\circ = 11.7° \pm 0.05°$ from the fitting procedure. The knockdown factor for this shell was measured experimentally to be $\kappa_d = 0.42 \pm 0.01$ using a standard buckling test (Lee et al., 2016b), in good agreement with the FEM prediction of 0.43. This difference is due to the uncontrollable imperfections intrinsic to the fabrication technique. The details about the procedure of the buckling test and the FEM framework can be found in our previous work (Lee et al., 2016b). Additional information on our numerical simulations will also be provided in Section 4. In Section 5, we will present the results of indentation tests on this shell specimen.

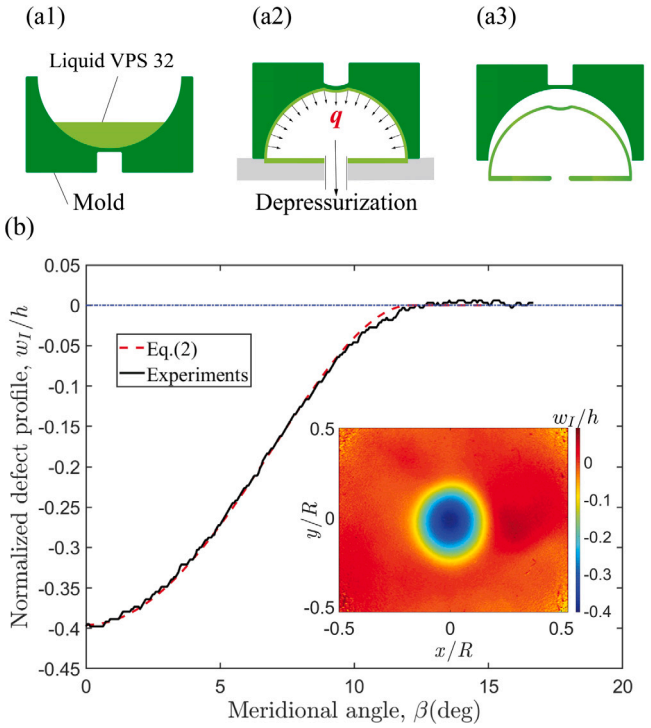

Fig. 2. (a) Schematic diagrams of the experimental protocol employed in the fabrication of thin hemispherical shells containing a geometric defect (Yan et al., 2021). (a1) First, a negative spherical mold with a thin region at the pole was filled with liquid VPS. (a2) The mold was then coated by the gravity–driven viscous flow of VPS, yielding a thin film on the mold. During the curing of the polymer solution, the elastic mold was depressurized to deflect the thin region, thus producing a geometric defect in the shell. (a3) Finally, upon curing, the shell was peeled off from the mold. (b) Characterization of the defect geometry. Two-dimensional profile (solid line) of the dimple-like defect w_I, normalized by shell thickness h, versus meridional angle β, obtained by averaging the measured 3D defect profile, latitude–wise, using an optical profilometer (see the inset). The dashed line represents the analytical description of Eq. (2). These results correspond to a representative shell contained a defect that was measured to have a normalized amplitude of $\bar{\delta} = 0.4 \pm 0.02$ and half angular width of $\beta_\circ = 11.7° \pm 0.05°$. The results from a systematic exploration of shells with other design parameters will be presented later in this manuscript.

3.3. Experimental apparatus and protocol

In Fig. 3, we present a photograph of the experimental apparatus used to perform the probing tests on our imperfect shells, based on earlier experiments developed by Marthelot et al. (2017). The to–be–tested hemispherical shell was mounted onto an acrylic plate. Clamped boundary condition at the equator were ensured by the thick band at the bottom of the shell (approximately 5 mm thick) formed by the drainage of excess polymer during fabrication. The gap between the rim of the specimen and the acrylic plate was sealed by VPS polymer poured around the thick band to ensure air tightness. The acrylic plate was then fixed onto a high–precision multi–angle mount (Arca-Swiss C1 Cube Geared Head, France), adopted to adjust the position and direction of indentation. The shell was connected to a syringe pump (NE-1000, New Era Pump Systems Inc., Farmingdale, NY), which extracted air from inside the shell, through the pneumatic circuit, at a rate of 0.1 mL/min to generate a negative pressure on the shell. A pressure sensor (MPXV7002, NXP Semiconductors, The Netherlands) monitored the pressure differential between the inside and the outside of the shell, $p_\circ$, at an acquisition rate of 1 Hz. The pneumatic circuit also contained a tank with a large volume of air ($V = 120$ L), serving as a buffer to ensure prescribed pressure conditions and minimize spurious variations of pressure during the indentation procedure. The level of fluctuations of $p_\circ$ during the indentation test was kept below 3% for larger pressures (above 30 Pa) and below 15% for lower pressures (below 30 Pa).

In each experimental run, we first loaded the shell to a preset pressure level, $p_\circ$, using the syringe pump. Once the desired pressure value was reached, the shell was indented by a rigid spherical Rockwell C diamond indenter (tip radius $a = 200\,\mu$m, CSM) mounted onto a universal testing machine (5943, Instron, Norwood, MA). This point–indentation force was consistently applied in the radial direction (perpendicular to the shell surface), either at the pole of the shell (where the defect is located) or at an angle between the direction of the indentation force and the radial line perpendicularly concentric to the defect (θ). The indentation displacement ξ was imposed by the testing machine (rigid probe) at a constant velocity of 0.06 mm/s. The reaction force of the indenter (indentation force), F, was measured by a load cell (2530-5N, Instron). During data processing, the zero point of the indentation displacement was set at the moment of contact between the indenter and the shell, after which the reaction force increased continuously.

Following previous studies (Hutchinson and Thompson, 2017b; Marthelot et al., 2017), we non-dimensionalize the indentation deflection as

$$\bar{\xi} = \sqrt{1-\nu^2}\,\frac{\xi}{h}\,. \tag{3}$$

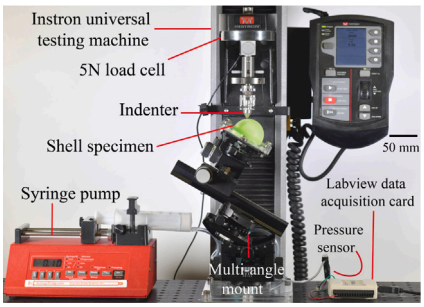

Fig. 3. Photograph of the experimental apparatus used for the indentation tests. In each experimental run, the shell was first depressurized to a prescribed pressure level and then indented under imposed displacement conditions by a universal testing machine. A high–precision multi–angle mount allowed for the indentation to be performed at different locations of the shell.

and the probe force as

$$\overline{F} = \frac{FR}{2\pi D}, \tag{4}$$

where $D = Eh^3/12(1-\nu^2)$ is the bending modulus of the shell. Moreover, the prescribed pressure level, p_o, at which the indentation test was performed, is normalized by the classic buckling pressure, p_c from Eq. (1), as

$$\overline{p} = \frac{p_o}{p_c}. \tag{5}$$

The buckling of thin spherical shells is dominated by the local region near the defect (Hutchinson and Thompson, 2018), which, in our study, is located at the north pole, away from the equator. The deformation caused by indentation is also localized near the indenter set in the vicinity of the north pole which will be elaborated in Section 5.3. As such, the effect of boundary conditions at the equator on critical buckling pressure and indentation behavior should be negligible (Hutchinson, 2016). We can expect the results presented in this work on hemispherical shells clamped at the equator should be equally applicable to full spherical shells as buckling is confined to the vicinity of the pole such that, if the shell is not shallow, the buckling thresholds are not strongly dependent on the location of the clamping boundary (Sieber et al., 2020)

For the indentation tests, we used the shell fabricated and characterized following the procedures described in Sections 3.1 and 3.2, respectively. Prior to indentation, the shell was preset at prescribed pressure levels, which were varied systematically in the range $0 \le \overline{p} < p_{max}/p_c$ (recalling that p_{max} is the critical buckling pressure measured in a standard buckling test). From the recorded indentation force–displacement curves, $\overline{F}(\overline{\xi})$, we attempted to assess the stability of the shell. The results for the case of indentation at the pole of the shell ($\theta = 0°$) will be provided in Section 5.1. Non-axisymmetric cases will be considered in Section 5.2, for indentation tests conducted at the following values of the probe angle: $\theta = \{5°, 10°, 12°, 15°, 30°\}$.

4. Numerical simulations using the finite element method

In parallel to the experiments, we followed the finite element method (FEM) to perform simulations using the commercial package Abaqus/Standard. The goal of these simulations was to predict the response of imperfect spherical shells under simultaneous pressure loading and indentation, as well as to explore parameters more systematically than those available through experiments. Toward reducing computational costs, we exploited the symmetry of the system and only considered one–half of the hemispherical shell (hence, a quarter of the shell), with symmetric boundary conditions applied on the plane of symmetry. The equator of the shell was set as a clamped boundary. A geometric defect (with the profile described by Eq. (2) and the amplitude and width characterized in Section 3.2) was introduced into the initial shell geometry. The VPS polymer was modeled as an incompressible neo-Hookean material, with a Young's modulus of $E = 1.26 \pm 0.01$ MPa measured from standard tensile tests on dog–bone specimens and the Poisson's ratio was assumed to be $\nu \approx 0.5$. The shell was discretized by four–node shell elements S4R with a structured mesh scheme, with 300 and 600 elements in the meridional and azimuthal directions, respectively. The element S4R is able to describe the finite membrane strains and arbitrarily large rotations of shells. A mesh convergence study was also implemented to ensure that the results were independent of the mesh size. We modeled a rigid indenter discretized by R3D4 rigid elements to apply the indentation under imposed displacements. A hard and frictionless contact was assigned between the indenter and the shell. Geometric nonlinearities were taken into account throughout the simulations.

The simulations were implemented in two steps:

(i) **Depressurizing**: First, the shell was loaded by a uniform live pressure applied on its outer surface, $\overline{p}$;
(ii) **Indentation**: While maintaining the pressure $\overline{p}$ set in step (i), the indentation displacement ($\overline{\xi}$) was then imposed onto the shell at a probe angle θ. The indentation force $\overline{F}$ was computed from equilibrium.

For each pressure level explored, we obtained the probe force–displacement curve and the full displacement field of the shell.

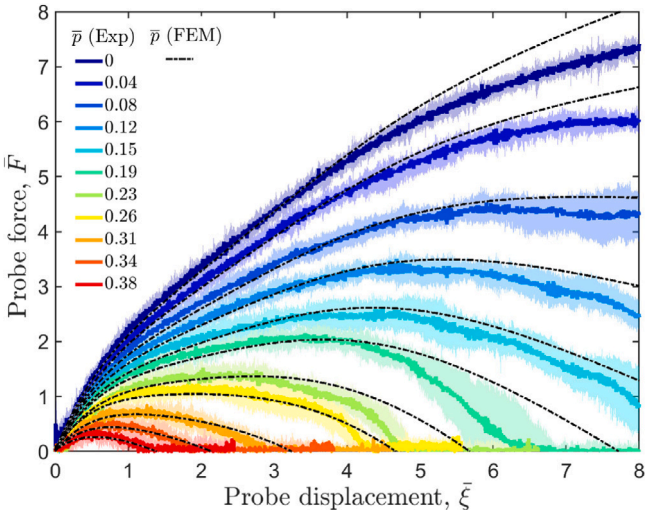

Fig. 4. Force–displacement curves for the indentation of the hemispherical shell. The normalized probe force, $\overline{F} = FR/(2\pi D)$, is plotted as a function of the normalized indentation displacement, $\overline{\xi} = \sqrt{1-\nu^2}\xi/h$. The indentation was applied at the center of the defect ($\theta = 0°$): experiments (solid lines) and FEM simulations (dashed lines). The indentation tests were performed at 11 levels of depressurization (see legend). Each solid line was obtained by averaging the results from 6 independent experimental runs under identical conditions. The corresponding shaded region associated with each curve represents the standard deviation of these 6 identical measurements. The dashed lines are predictions from the FEM simulations associated with the respective experimental curves, with no fitting parameters; all quantities were measured from the experiments.

5. Results

We shall start our investigation by reporting, in Section 5.1, results on the response of depressurized spherical shells subjected to an indentation applied at the center of the dimple–like defect. Upon validating our FEM procedure by contrasting the numerical results against experiments, in Section 5.2, we perform probing measurements and simulations at different probe angles. From the results, we seek to analyze the effect of the probe angle on predicting the critical buckling conditions of the shell and examine the efficacy of indentation as a technique to assess the shell stability. Finally, in Sections 5.3 and 5.4, we study the localized deformation of spherical shells resulting from indentation. Furthermore, adapting well–established results from classic shallow shell theory, we quantify the characteristic length of this deformation. The shallow shell equations are applicable to this case (and to deep shells), as long as the loads and the resulting stresses are restricted to shallow regions, where the indentation–induced dimple is localized in the neighborhood of the indenter (Hutchinson and Thompson, 2017b). Moreover, outside of this region, the stresses and strains due to indentation and depressurization are sufficiently small compared to those in the dimple, such that the predictions of shallow shell theory remains relevant.

5.1. Probing the shell at the center of the defect

In Fig. 4, we present a set of experimental results for the response of the probe force versus the displacement of indenter applied onto the shell. For now, the indentation point located at the center of the dimple–like defect ($\theta = 0°$; cases with $\theta > 0°$ will be explored in Section 5.2). The prescribed depressurization was systematically varied at 11 values, ranging from $\overline{p} = 0$ to $\overline{p} = 0.38$. The maximum imposed displacement of the indentation was $\overline{\xi} = 8$. At each value of $\overline{p}$, in order to enhance the signal-to-noise ratio, 6 independent, but otherwise identical, experimental runs were conducted and the measured indentation forces were averaged to yield the $\overline{F}(\overline{\xi})$ curve presented in Fig. 4. The corresponding shaded region is the standard deviation of these 6 measurements.

From the results shown in Fig. 4, as previously described by Marthelot et al. (2017), we notice that, without pressure loading ($\overline{p} = 0$), the indentation process is always stable and the probe force increases monotonically with displacement. Each response at lower values of the pressure loading ($\overline{p} < 0.08$) can be divided into the following two distinct regimes:

1. **Small indentations** ($\xi \lesssim h$): In this regime, the indentation displacement remains smaller than the shell thickness. The force–displacement relationship is linear, as described by Reissner's theory for spherical shells under point load indentation (Reissner, 1946a,b);
2. **Large indentations** ($\xi \gtrsim h$): In this regime, the indentation displacement is larger than the shell thickness. The force–displacement relationship is nonlinear, as first studied by Pogorelov (1988).

For intermediate levels of depressurization ($0.12 \leq \overline{p} \leq 0.19$), the indentation curve is non-monotonic; the probe force increases initially, reaches a maximum value $\overline{F}_{\max}$, and then decreases with increasing probe displacement. For levels of depressurization

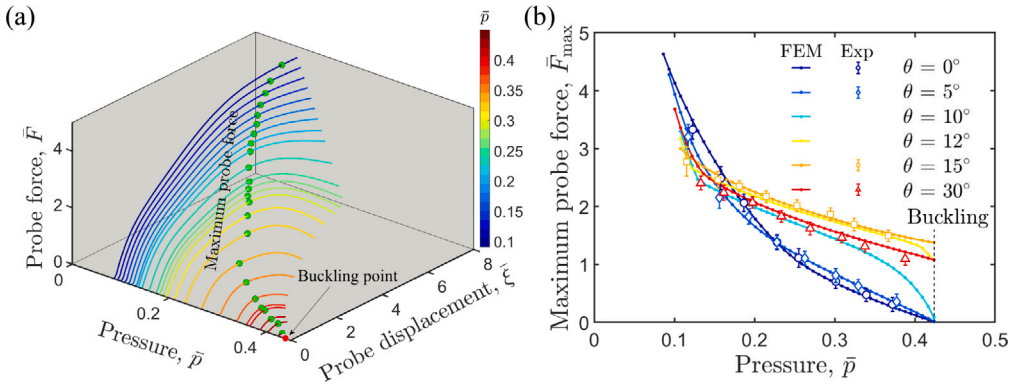

Fig. 5. (a) 3D representation of the indentation curves shown in Fig. 4, in the ($\bar{p}$, $\bar{\xi}$, $\bar{F}$) space. The peak values of the probe force, $\bar{F}_{max}$, are represented by the circles on each curve. The indentation was performed at the center of the defect ($\theta = 0°$). (b) Normalized maximum probe force, $\bar{F}_{max}$, versus the prescribed pressure, $\bar{p}$, at different probe angles: $\theta = \{0°, 5°, 10°, 12°, 15°, 30°\}$. The data points represent the experimental measurements and the solid lines are the predictions from the FEM simulations. The knockdown factor of this shell measured through an independent buckling test is $\kappa_d = 0.42$.

above $\bar{p} \geq 0.19$, the probe force can eventually reach zero within the indentation displacement range of the experiments. At this point, the shell becomes unstable (critical buckling point) and snaps to a collapsed state. The work done by the probe force is equal to the energy barrier that needs to be overcome to attain the buckled state. Also, it is important to mention that, compared to a perfect shell (Hutchinson and Thompson, 2017b; Marthelot et al., 2017), the load–carrying capacity and energy barrier of this imperfect shell are significantly reduced due to the presence of the dimple-like defect.

Following the computational methodology described in Section 4, we have used FEM to predict the behavior of this shell under indentation, and the obtained force–displacement curves at different pressure levels are also presented in Fig. 4, juxtaposed onto the corresponding experimental curves. Excellent agreement is found between experiments and simulations, thereby serving as a validation of the FEM. We note that all the parameters used in the simulations were measured independently from the experiments, with no fitting parameters. Having validated the FEM against experiments, we will further explore the indentation problem by performing systematic computations in Sections 5.2 and 5.3.

5.2. *Can we use indentation as a non-destructive technique to probe the critical buckling conditions of spherical shells?*

In this section, we will assess the relevance of the non-destructive probing technique to predict the critical load of pressurized spherical shells, which was originally proposed and applied on cylindrical shells (Yadav and Gerasimidis, 2020; Yadav et al., 2021; Virot et al., 2017; Kreilos and Schneider, 2017; Thompson, 2015; Hutchinson and Thompson, 2017b; Thompson and Sieber, 2016; Thompson et al., 2017). We seek to determine the required proximity of the probe to the defect without the foreknowledge on the location and size of imperfections. In particular, we will apply the probe at various locations on the shell by moving the indentation point away from the center of the defect and quantify the resulting response, both experimentally and numerically.

In Fig. 5a, we present the FEM results for the indentation at $\theta = 0°$ (from Fig. 4) in the ($\bar{p}$, $\bar{\xi}$, $\bar{F}$) space. The maximum probe force, $\bar{F}_{max} = F_{max} R/2\pi D$, provides a measure of the largest load that the shell can sustain prior to collapse, which can be tracked at increasing pressure levels (green circles on each curve in Fig. 5a). It is anticipated that the characteristics of shell stability, such as the critical load, are encoded in the variation of $\bar{F}_{max}$ (Virot et al., 2017). More precisely, the energy barrier, which measures the shock-sensitivity of the pressurized shell against disturbances at the pre-buckling state, is equal to the work done by the probe to reach the unstable post-buckling state (Thompson and Sieber, 2016). Once this work tends to vanish, the shell is loaded close to the buckling capacity. By sequentially increasing the prescribed pressure until $\bar{F}_{max} = 0$, the pressure level reached at this stage corresponds to the critical buckling load of the shell. However, in practice, we should always ensure that $\bar{F}_{max}$ is larger than zero to avoid catastrophic collapse of the tested shell. Therefore, we identify the critical point by numerically extrapolating the experimental measured $\bar{F}_{max}$ to zero, using a third order polynomial extrapolation.

In Fig. 5b, we plot $\bar{F}_{max}$ versus $\bar{p}$ while probing the shell at the center of the defect ($\theta = 0°$). The experimental force–displacement signals were filtered and smoothed with a 50-point moving average filter in order to facilitate the definition and extraction of the maximum probe force. We find that $\bar{F}_{max}$ decreases sharply (by 80%) as $\bar{p}$ is increased from 0.1 to 0.43. The extrapolation in the limit of $\bar{F}_{max} \to 0$ indicates that $\kappa_d = 0.44$, which is in good agreement with the value $\kappa_d = 0.42$ measured from an independent experimental buckling test. In this case of indentation at the center of the defect, the probing serves successfully as a non-destructive technique to estimate the critical buckling conditions of the spherical shell. We note that, based on the FEM data, we systematically set an upper limit on the pressure applied for probing, p_{lim}, and extrapolated the critical point from the maximum probe forces obtained below this limit. This allowed us to have determined a threshold $p_{lim}/p_c = 0.36$, above which the extrapolated buckling

load is excellent, approaching the measured value with less than 2% relative error. This pressure threshold is still in the safe region (far from $\kappa_d = 0.43$) to avoid collapse of the shell caused by the probe.

To assess the ability of the probing technique when the indentation is exerted at various locations, we systematically varied the probe angle: $\theta = \{5°, 10°, 12°, 15°, 30°\}$. Consequently, the indentation point was moved away from the center of the defect. First, we indented the shell at $\theta = 5°$, the results of which are shown in Fig. 5b. The probe force follows a path that only slightly deviates from that of the $\theta = 0°$ case, while still showing a similar trend, and decreases to zero as the prescribed pressure reaches the critical load of the shell. In this case, the knockdown factor can still be accurately inferred.

Next, we increase the probe angle to $\theta = 10°$. Initially, with increasing $\overline{p}$, the maximum probe force evolves by following an entirely distinct path from the previous two cases ($\theta = 0°$ and $\theta = 5°$). However, closer to the load-carrying capacity of the shell, the path rapidly turns and drops to the critical point. Again, in this case, the correct knockdown factor can be inferred from the probing. However, the extrapolation must be performed based on the data in the nonlinear vicinity of the critical point, with the eminent risk of buckling. We highlight that this extrapolation cannot be done from the beginning of the $\overline{F}_{max}(\overline{p})$ path. The sudden change of the maximum force–pressure path and the sharp decrease in $\overline{F}_{max}$ for larger pressure values in the cases of $\theta = 10°$ and $\theta = 12°$ (half angular width of the defect = 11.7°) is presumably due to the nonlinear interaction between the probe and the edge of the defect.

Further increasing the distance of the probing point from the defect ($\theta = 15°$ and $\theta = 30°$), we observed no visible trace of the defect in the force signal until $\overline{p}$ approaches the critical pressure with the sudden collapse of the shell. In these two cases, the buckling point and the corresponding knockdown factor are unpredictable by tracking the maximum probe force and extrapolating it in the limit $\overline{F}_{max} \to 0$. The probe for these indentations, away from the defect, appears to be insensitive to the defect and misrecognizes the imperfect shell as if it was perfect.

An interesting result, which was also alluded to by Marthelot et al. (2017), was observed when the indentation was applied at $\theta = 12°$ and $\theta = 15°$. There is an unexpected increase in the maximum indentation force that the shell can sustain, compared to that at $\theta = 30°$. In this regime, the probe is set at the edge of the defect and the coupling between the localized deformation associated with the dimple-like defect and the probe force is more complex; the indentation deforms the shell locally in a way that weakens the influence of the initial imperfection on the response of the shell. This observation highlights the high degree of nonlinearity in shell mechanics problems.

We highlight that the experimental data and FEM results plotted in Fig. 5(b), at different probe angles, are in remarkably good quantitative agreement. In summary, the results presented above demonstrate some potential limitations in using probing as a non-destructive technique to assess the stability of imperfect spherical shells, since the probe has to be performed in the near vicinity of the most serious defect in the shell, whose location would be most likely unknown *a priori* in any situation of practical relevance. Indeed, performing such a positionally targeted test would require previous knowledge of the distribution of imperfections, in which case the behavior of the shell could be more easily and accurately predicted numerically by taking the full shell geometry into account (Lee et al., 2016b; Yan et al., 2020b; Pezzulla and Reis, 2019). The mechanism underlying these observations stems from the fact that the deformation due to the probe force is localized in spherical shells, as we study in detail in the next section. The interaction between the localized probe and the defect is limited, which affects the detectability of the defect.

5.3. Localized deformation of pressurized spherical shells under indentation

Thus far, we provided experimental and numerical evidence that the mechanical response of pressurized spherical shells under point indentation differs strongly depending on the location of the probing, with respect to the most vulnerable (imperfect) region. In this section, we will relate this finding to the deformation profiles of the imperfect shells due to indentation.

In Fig. 6, we plot the FEM–simulated profile of the imperfect shell tested in Sections 5.1 and 5.2, at $\overline{p} = 0.25$, before and after imposing an indentation displacement of $\overline{\xi} = 3$. This probing is applied at the following different angles $\theta = \{0°, 5°, 15°, 30°\}$. We find that, when the shell is indented at or close to the center of the defect ($\theta = \{0°, 5°\}$), the localized region of deformation overlaps almost entirely with the dimple-like defect. Consequently, the defect significantly influences the response of the shell due to the indentation, thereby ensuring that the critical point can be captured by the probe. By contrast, when the probing is performed further away from the defect (*e.g.*, $\theta \leq 15°$), there is little or no overlap between the deformed region and the existing defect, and the probe misses the detection of the critical buckling point. As a result, for these cases of indentation away from the defect, the corresponding $\bar{F}(\bar{p})$ curves (Fig. 5b) show little different with respect to those of a perfect shell, even if the probed shell is intrinsically imperfect. In these cases, the lack of interaction between the defect and the probe precludes access to the stability landscape of the imperfect shell.

5.4. Characteristic length of indentation in spherical shells

Having observed that the deformed neighborhood of the indentation plays an important role in the interaction between the probe and the defect, we proceed by quantifying the characteristic length scale of deformation of the indented shells. In this section, we shall focus exclusively on perfect shells so as to investigate their mechanical response to indentation independently of any interactions with geometric defects. The experimental shell specimen used in this section was fabricated without intentionally introducing a defect, so that it is as nearly '*perfect*' as they can be in practice. Naturally, there may still be small–scale imperfections

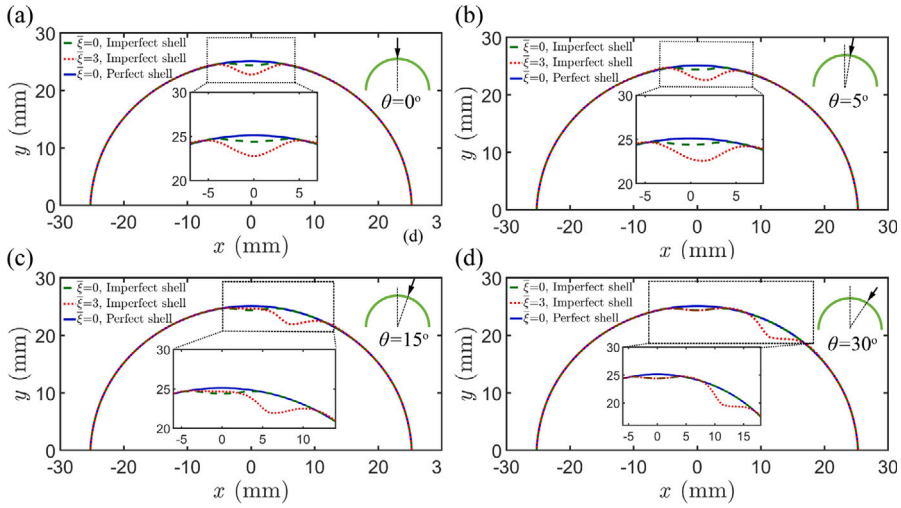

Fig. 6. Deformation profiles of the imperfect shell, pressurized at $\bar{p} = 0.25$, in its initial configuration ($\bar{\xi} = 0$, dashed line) and deformed configuration (at $\bar{\xi} = 3$, dotted line), computed through FEM. The indentation is applied at (a) $\theta = 0°$, (b) $\theta = 5°$, (c) $\theta = 15°$, and (d) $\theta = 30°$. To aid visualization, the deformation profiles of the indented imperfect shell are represented by the associated radial displacement from a perfect spherical shell pressurized at the same level (solid line), and magnified by a factor of 4. Insets: Zoomed-in profiles at the vicinity of the defect and indentation region.

intrinsic to the fabrication procedure (*e.g.*, roughness of the otherwise spherical mold or heterogeneities in the polymer mixture). In fact, the knockdown factor of these nearly perfect shells is $k_d = 0.91$ (instead $k_d = 1$ for a perfect shell), which, nonetheless, does not affect the findings reported in this section. The FEM simulations are performed with a truly spherical shell.

We will contrast our experimental and FEM data with classic analytical solutions obtained by Reissner (1946a,b) and Pogorelov (1988) for a segment of a thin, elastic, spherical shell subjected to a concentrated point force. Reissner's solution was obtained from simplified shallow shell equations (relevant for shells with a height-to-diameter ratio lower than approximately 1/8). Such equations are linearized, but some important nonlinear terms related to buckling were preserved. These equations are also applicable to deep shells, as long as the loads and the resulting stresses are restricted to (*i.e.*, localized in) shallow regions. For completeness, we recall the main features of these seminal results on shell indentation:

1. ***Linear regime*:** When $\xi/h \lesssim 1$, Reissner (1946a,b) followed the framework of linear shallow shell theory to proposed an analytical solution for the radial displacement:

$$\frac{w_{\text{Reissner}}(r)}{h} = \frac{\sqrt{12\left(1-\nu^2\right)}}{2\pi}\frac{R}{h}\frac{F}{Eh^2}\,\text{kei}\left(\frac{r}{\ell}\right), \tag{6}$$

where r is the horizontal distance from a point on the shell to the point of application of the concentrated point force F, kei(·) is the imaginary term of the modified Bessel–Kelvin function, and the balance between bending and stretching effects yields the characteristic length scale $\ell = [\sqrt{Rh}]\left[12\left(1-\nu^2\right)\right]^{-1/4}$. Therefore, at the indentation point ($r = 0$), the deflection is predicted to be

$$\frac{\xi}{h} = \frac{w_{\text{Reissner}}(0)}{h} = -\frac{\sqrt{3\left(1-\nu^2\right)}}{4}\frac{R}{h}\frac{F}{Eh^2}, \tag{7}$$

such that the dependence between the indentation force and displacement is linear ($F \sim \xi$).

2. ***Nonlinear regime:*** When $\xi/h \gtrsim 1$, Pogorelov (1988) made use of geometric arguments and a general variational principle to obtain an analytical solution for the radial displacement at the indentation point, $w_{\text{Pogorelov}}(0)$:

$$\frac{\xi}{h} = \frac{w_{\text{Pogorelov}}(0)}{h} = \frac{1}{9\pi^2 c^2}\left(\frac{R}{h}\right)^2\left(\frac{F}{Eh^2}\right)^2, \tag{8}$$

where $c = 0.19$ is a numerical coefficient. Eq. (8) indicates a nonlinear indentation force–displacement relationship of $F \sim \sqrt{\xi}$. Pogorelov developed this approach to describe the behavior of thin spherical shells under point indentation, with considerable changes in shape, based on the assumption that the shell's middle surface under such a deformation is close to the isometric mapping of the initial surface. The shape of the shell in the transition zone between the undeformed and mirror–reflected parts is determined by minimizing the strain energy in this region due to the smoothing of the edge between the two parts (computed according to the linear membrane and bending strains), under appropriate boundary conditions. The indentation force–displacement relationship of the shell is then obtained from the minimization of the total potential energy of the system.

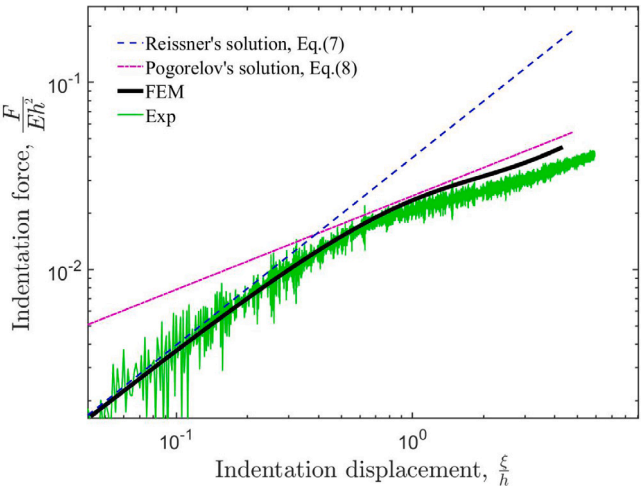

Fig. 7. Force–displacement curves for a spherical shell indented at its pole ($\theta = 0°$): experiments (thin solid curve), FEM simulations (thick solid curve). The predictions from Reissner's theory (Reissner, 1946b), Eq. (7), and Pogorelov's theory (Pogorelov, 1988), Eq. (8), are represented by the dashed and dash-dotted lines, respectively.

In Fig. 7, we plot experimental and FEM results for the dimensionless indentation force, $\bar{F} = F/(Eh^2)$, versus the normalized indentation displacement, ξ/h, for a shell indented at its pole ($\theta = 0°$), in the absence of pressure loading. Linear (when $\xi \lesssim h$) and nonlinear (when $\xi \gtrsim h$) regimes can be clearly identified in this force–displacement curve. The transition from the linear to the nonlinear regimes does indeed happen in the range $0.3 \lesssim \xi/h \lesssim 0.5$, consistently with the classic result of $\xi < h/3$ for the validity of linear shell theory. However, since the transition is smooth, we prefer to stick with the less precise statement that the transition between the two regimes happens when the indentation amplitude is of order h.

The classic analytical predictions of Eqs. (7) and (8), for the linear and nonlinear regimes, respectively, are superimposed onto our data. As expected, Reissner's solution yields excellent predictions in the linear range, while the nonlinear range is well described by Pogorelov's solution, in both cases without any adjustable fitting parameters.

Having thoroughly validated our simulations against experiments (see Figs. 4, 5b, and 7), hereon, we shall rely exclusively on the FEM data. We have studied the extent of deformation due to indentation in the linear and nonlinear regimes, from which we observed the deformation is concentrated at the indentation point and decays rapidly away from it (See Appendix A). As such, we can focus on the case of indentation at the pole ($\theta = 0^o$) and characterize the neighborhood of indentation by the zero crossing distance r_z, which is defined as the distance from the center of indentation to the first point of $w(r_z)/R = 0$ (see Appendix B for details). This characteristic length quantifies the localized nature of indentation of spherical shells.

In the FEM simulations, we considered shells with different radius-to-thickness ratios ($64 \le R/h \le 121$) and extracted r_z from their deflection profiles under various indentation displacements. We also obtained a theoretical prediction from Reissner's solution, Eq. (6), by setting $w_{\text{Reissner}}(r_z) = 0$, which is satisfied only if $\text{kei}(r_z/\ell) = 0$. Then we numerically determined the first zero-crossing point as

$$r_z = \frac{3.9}{\left[12(1-\nu^2)\right]^{1/4}}\sqrt{Rh}\,. \tag{9}$$

For incompressible materials ($\nu = 0.5$), we have $r_z = 2.25\sqrt{Rh}$. From Eq. (9), the characteristic length of indentation is predicted to scale as $r_z \sim \sqrt{Rh}$, independently of the indentation displacement, ξ.

In Fig. 8, we plot r_z data obtained by FEM as a function of $\sqrt{Rh}$, contrasted with Eq. (9); the line colors refer to the values of the indentation displacement in FEM (as detailed in the legend). For clarity the data was split for the linear regime ($0 < \xi \lesssim h$, Fig. 8a) and for the nonlinear regime ($\xi \gtrsim h$, Fig. 8b). In the linear regime (Fig. 8a), good agreement is found between FEM and Eq. (9), validating the linear dependence of characteristic length, $r_z \sim \sqrt{Rh}$, even if there is a slight systematic vertical shift for the FEM data from Reissner's theory that increases with ξ. We anticipate that this discrepancy is most likely due to the simplification of linear shallow shells in Reissner's solution. When $\xi \gtrsim h$ (Fig. 8b), the perturbed region of radius r_z grows more significantly with indentation, but the linear scaling $\sqrt{Rh}$ is maintained. Hence, Reissner's solution is unable to capture our FEM data in the nonlinear regime. Overall, we find that the measured characteristic length of indentation is consistent with the scaling $r_z \sim \sqrt{Rh}$, with a nearly constant prefactor of 2.25 in the linear regime but an indentation-dependent prefactor in the nonlinear regime.

For the shell tested in our experiments, Eq. (9) yields a characteristic length of indentation $r_z = 6.5\,\text{mm}$, corresponding to an angle of $\theta_z = 14.8°$. From all the evidence reported above, we speculate that θ_z, together with the half angular width of the defect $\beta_o = 11.7°$, dictates the critical indentation angle, above which the probing test fails to identify the buckling conditions. In future

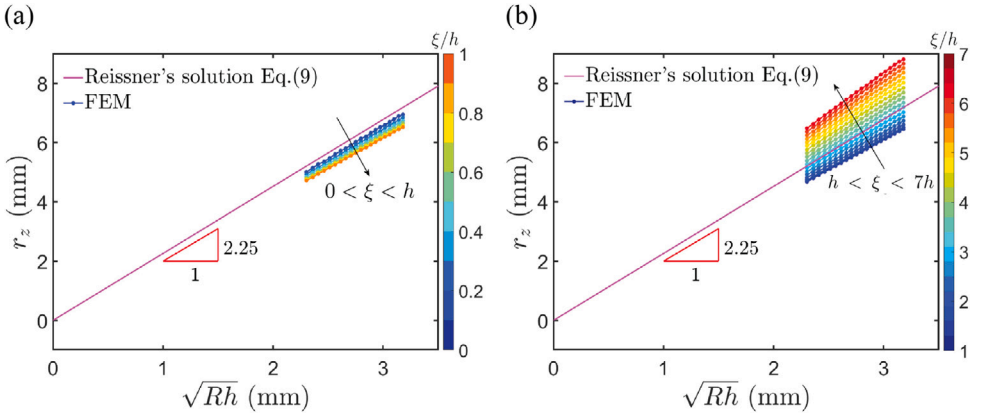

Fig. 8. Characteristic length of indentation, r_z, as a function of $\sqrt{Rh}$ in the (a) linear ($0 < \xi < h$) and (b) nonlinear ($\xi \gtrsim h$) regimes. The solid lines correspond to the theoretical predictions of Eq. (9), with a slope of 2.25, and colored circles-lines correspond to the FEM data for different values of the indentation displacement (ξ/h); see adjacent color bar.

work, it would be valuable to perform a parametric study to more systematically quantify the dependence of the critical indentation angle on both the length scale of indentation and the geometry of defects.

6. Conclusion

We have investigated the behavior of imperfect spherical shells subjected to a point indentation, with a focus on the effect of the indentation angle, by performing precision experiments, finite element modeling, and theoretical analyses. When the indentation is applied at the center of the defect under imposed displacement conditions, the reaction force shows a non-monotonic relationship with the displacement at relatively larger pressure levels, which first increases to a peak value and then decreases to zero accompanied by the occurrence of buckling. The knockdown factor of the shell is successfully identified by tracking the peak of force–displacement curve with increasing prescribed pressure level and extrapolating to the point of maximum force reaching zero. In this case, indentation can be used to probe the stability of the shell. However, as the probe is moved away from the center of the defect above a critical angle, the test fails to identify the buckling point prior to the collapse of the shell. We find that the localized nature of indentation in spherical shells limits the interaction between the defect and the probe. The characteristic length associated with the indentation's neighborhood scales as $r_z \sim \sqrt{Rh}$, in both the linear and nonlinear regimes.

Our findings demonstrate that point–load probing can only be useful as a local strategy to assess the stability of spherical shells, as long as the indentation is performed in the close neighborhood of the defect. This limitation compromises broader applications in common engineering settings, where the distribution and magnitude of the imperfections is typically unknown. The counterpart evaluation on cylindrical shells (Yadav and Gerasimidis, 2020; Yadav et al., 2021) through FEM and experiments also showed that the probing technique over–predicts the buckling load, once the distance between the probe and the defect reaches a critical value. It would be interesting to study the characteristic length of the influence region of indentation in cylindrical shells, as we have performed in this paper on spherical shells. As we have done in our case of spherical shells, we can also expect that this length should determine the detectability of the probe in cylindrical shells.

Future work could consider simultaneously setting multiple probes on one shell or implementing probing in sequence along an effective path, although such indentation–probing approaches would likely be cumbersome. A more viable route to predict the critical buckling conditions may be the mapping of the full 3D geometry of an imperfect shell through X-ray micro computed tomography coupled with FEM simulations using the measured geometry, as we have recently demonstrated for idealized single-defect imperfections (Lee et al., 2019; Yan et al., 2021). An appropriate and effective protocol is still to be developed for the non-destructive testing of the critical buckling conditions of imperfect spherical shells in general engineering scenarios. We hope our present work will stimulate future studies in this direction.

CRediT authorship contribution statement

Arefeh Abbasi: Conceptualization, Investigation, Validation, Methodology, Formal analysis, Software, Writing - original draft, Writing - review & editing. **Dong Yan:** Conceptualization, Methodology, Software, Writing - review & editing. **Pedro M. Reis:** Conceptualization, Methodology, Supervision, Writing - review & editing.

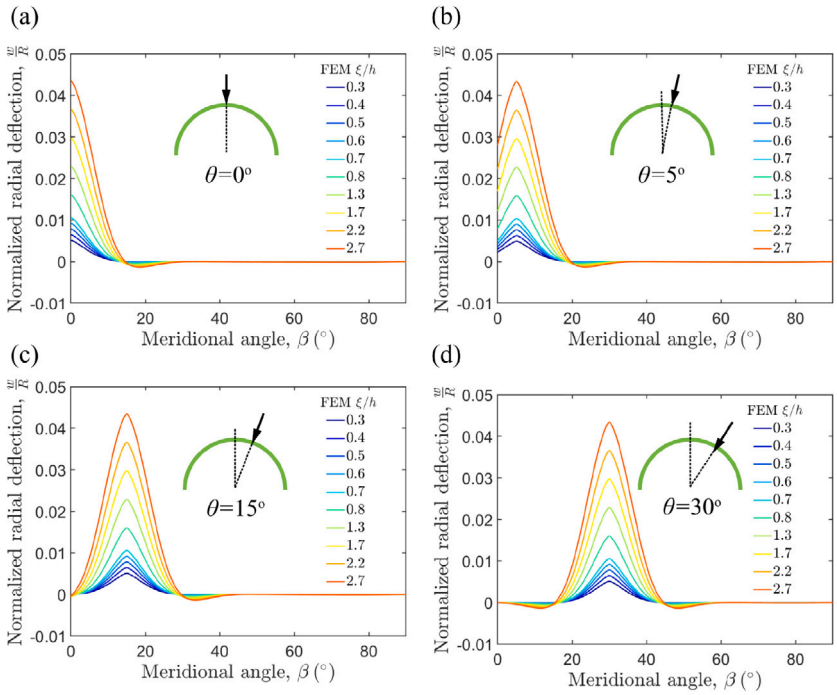

Fig. A.9. FEM–computed normalized radial deflection, w/R, versus meridional angle, β, for a perfect shell with $R = 25.4\,\text{mm}$ and $h = 327\,\mu\text{m}$, under different indentation displacements (values detailed in the legends). The probing is applied at the following values of the indentation angle: (a) $\theta = 0°$, (b) $\theta = 5°$, (c) $\theta = 15°$, and (d) $\theta = 30°$. For these data, no pressure loading is applied.

Declaration of competing interest

The authors declare that they have no known competing financial interests or personal relationships that could have appeared to influence the work reported in this paper.

Acknowledgments

A.A. is grateful to the support from the Federal Commission for Scholarships for Foreign Students (FCS), Switzerland through a Swiss Government Excellence Scholarship (Grant No. 2019.0619). We thank Matteo Pezzulla for fruitful discussions.

Appendix A. Localization of the indentation deformation

We study the extent of deformation due to indentation in the linear and nonlinear regimes, while systematically varying the indentation angle $\theta = \{0°, 5°, 15°, 30°\}$. In Fig. A.9, we plot the radial deflection of the shell, w/R, resulting from the indentation, as a function of the meridional angle, β. The indentation displacement was increased systematically up to $\xi = 2.7h$ (see the legend of Fig. A.9), across the linear and into the nonlinear regimes. The localized nature of the deflection profiles is evident from the data: The deformation is concentrated at the indentation point and decays rapidly away from it. The spatial extent of the deformed region only changes slightly for the different curves ($0 < \xi \leq 2.7h$) but remains independent of the indentation location ($\theta = \{0°, 5°, 15°, 30°\}$ in the respective panels of Fig. A.9).

Appendix B. Influence region of indentation

We focus on the case of indentation at the pole ($\theta = 0°$) and, in Fig. B.10b, plot w/R as a function of meridional distance r, against Reissner's solution from Eq. (6). It is evident that for displacements smaller than the shell thickness ($\xi \lesssim h$), Eq. (6) (dashed lines) is in excellent agreement with the FEM data (solid lines). However, deviations occur in the nonlinear regime ($\xi \gtrsim h$).

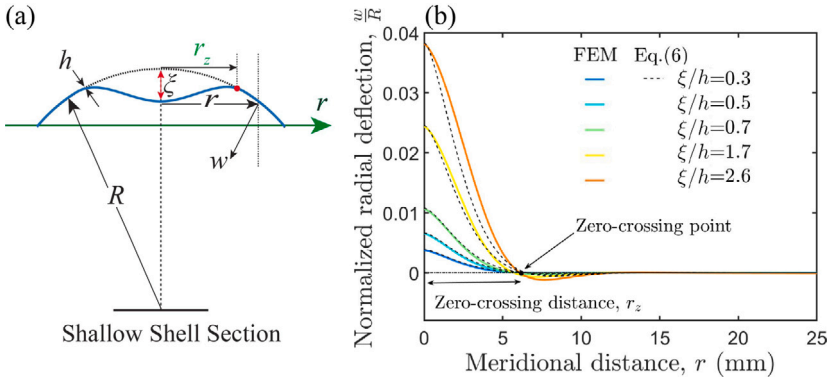

Fig. B.10. (a) Schematic of a deformed shallow spherical shell of radius R and thickness h under indentation. (b) Normalized radial deflection, w/R, as a function of meridional distance, r, for a shell of $R/h = 78$ at different indentation displacements (as detailed in the legend). The solid lines correspond to FEM data while dashed lines are predictions by Reissner's solution in Eq. (6). The zero–crossing distance, r_z, is defined as the distance from the center of indentation to the first point where the deflection crosses zero, $w(r_z)/R = 0$.

References

Abramian, A., Virot, E., Lozano, E., Rubinstein, S.M., Schneider, T.M., 2020. Nondestructive prediction of the buckling load of imperfect shells. Phys. Rev. Lett. 125 (22), 225504.

Babcock, C.D., 1983. Shell stability. J. Appl. Mech. 50 (4b), 935–940.

Baumgarten, L., Kierfeld, J., 2019. Shallow shell theory of the buckling energy barrier: From the Pogorelov state to softening and imperfection sensitivity close to the buckling pressure. Phys. Rev. E 99, 022803.

Bijlaard, P.P., Gallagher, R.H., 1960. Elastic instability of a cylindrical shell under arbitrary circumferential variation of axial stress. J. Aerosp. Sci. 27 (11), 854–858.

Budiansky, B., Hutchinson, J.W., 1972. Buckling of circular cylindrical shells under axial compression. In: Contributions to the Theory of Aircraft Structures. Delft University Press, The Netherlands, pp. 239–259.

Carlson, R.L., Sendelbeck, R.L., Hoff, N.J., 1967. Experimental studies of the buckling of complete spherical shells. Exp. Mech. 7 (7), 281–288.

Chen, W.L., 1959. Effect of Geometrical Imperfection on the Elastic Buckling of Thin Shallow Spherical Shells (Ph.D. thesis). Massachusetts Institute of Technology, Cambridge, MA.

Datta, S.S., Abbaspourrad, A., Amstad, E., Fan, J., Kim, S.-H., Romanowsky, M., Shum, H.C., Sun, B., Utada, A.S., Windbergs, M., 2014. 25th anniversary article: Double emulsion templated solid microcapsules: Mechanics and controlled release. Adv. Mater. 26 (14), 2205–2218.

Elishakoff, I., 2014. Resolution of the Twentieth Century Conundrum in Elastic Stability. World Scientific Publishing, Singapore.

Fan, H., 2019. Critical buckling load prediction of axially compressed cylindrical shell based on non-destructive probing method. Thin-Walled Struct. 139, 91–104.

Hilburger, M.W., 2012. Developing the next generation shell buckling design factors and technologies. In: 53rd AIAA/ASME/ASCE/AHS/ASC Structures, Structural Dynamics and Materials Conference. In: Structures, Structural Dynamics, and Materials and Co-located Conferences, American Institute of Aeronautics and Astronautics, Honolulu, HI.

Homewood, R.H., Brine, A.C., Johnson, A.E., 1961. Experimental investigation of the buckling instability of monocoque shells. Exp. Mech. 1 (3), 88–96.

Hutchinson, J.W., 2016. Buckling of spherical shells revisited. Proc. R. Soc. A 472 (2195), 20160577.

Hutchinson, J.W., Muggeridge, D.B., Tennyson, R.C., 1971. Effect of a local axisymmetric imperfection on the buckling behavior of a circular cylindrical shell under axial compression. AIAA J. 9 (1), 48–52.

Hutchinson, J.W., Thompson, J.M.T., 2017a. Nonlinear buckling behaviour of spherical shells: barriers and symmetry-breaking dimples. Phil. Trans. R. Soc. A 375 (2093), 20160154.

Hutchinson, J.W., Thompson, J.M.T., 2017b. Nonlinear buckling interaction for spherical shells subject to pressure and probing forces. J. Appl. Mech. 84 (6), 061001.

Hutchinson, J.W., Thompson, J.M.T., 2018. Imperfections and energy barriers in shell buckling. Int. J. Solids Struct. 148–149, 157–168.

Kaplan, A., Fung, Y.C., 1954. A Nonlinear Theory of Bending and Buckling of Thin Elastic Shallow Spherical Shells. Technical Note 3212, National Advisory Committee for Aeronautics, Washington, DC.

Karman, T.v., 1940. The influence of curvature on the buckling characteristics of structures. J. Aeronaut. Sci. 7 (7), 276–289.

Karman, T.v., 1941. The buckling of thin cylindrical shells under axial compression. J. Aeronaut. Sci. 8 (8), 303–312.

von Kármán, T., Tsien, H.-S., 1939. The buckling of spherical shells by external pressure. J. Aeronaut. Sci. 7 (2), 43–50.

Kobayashi, S., 1968. The influence of the boundary conditions on the buckling load of cylindrical shells under axial compression. J. Japan Soc. Aeronaut. Eng. 16 (170), 74–82.

Koiter, W.T., 1945. Over de Stabiliteit van Het Elastisch Evenwicht (Ph.D. thesis). Delft University of Technology, Delft, The Netherlands.

Kreilos, T., Schneider, T.M., 2017. Fully localized post-buckling states of cylindrical shells under axial compression. Proc. R. Soc. A 473 (2205), 20170177.

Krenzke, M.A., Kiernan, T.J., 1963. Elastic stability of near-perfect shallow spherical shells. AIAA J. 1 (12), 2855–2857.

Lee, A., Brun, P.-T., Marthelot, J., Balestra, G., Gallaire, F., Reis, P.M., 2016a. Fabrication of slender elastic shells by the coating of curved surfaces. Nature Commun. 7, 11155.

Lee, A., López Jiménez, F., Marthelot, J., Hutchinson, J.W., Reis, P.M., 2016b. The geometric role of precisely engineered imperfections on the critical buckling load of spherical elastic shells. J. Appl. Mech. 83 (11), 111005.

Lee, A., Yan, D., Pezzulla, M., Holmes, D.P., Reis, P.M., 2019. Evolution of critical buckling conditions in imperfect bilayer shells through residual swelling. Soft Matter 15 (30), 6134–6144.

López Jiménez, F., Marthelot, J., Lee, A., Hutchinson, J.W., Reis, P.M., 2017. Technical brief: knockdown factor for the buckling of spherical shells containing large-amplitude geometric defects. J. Appl. Mech. 84, 034501.

Marthelot, J., López Jiménez, F., Lee, A., Hutchinson, J.W., Reis, P.M., 2017. Buckling of a pressurized hemispherical shell subjected to a probing force. J. Appl. Mech. 84, 121005.

Pedersen, P.T., Jensen, J.J., 1995. Buckling behaviour of imperfect spherical shells subjected to different load conditions. Thin-Walled Struct. 23 (1), 41–55.
Pezzulla, M., Reis, P.M., 2019. A weak form implementation of nonlinear axisymmetric shell equations with examples. J. Appl. Mech. 84 (3), 034501.
Pogorelov, A.V., 1988. Bendings of Surfaces and Stability of Shells. In: (Translations of Mathematical Monographs), vol. 72, American Mathematical Society.
Reissner, E., 1946a. Stresses and small displacements of shallow spherical shells. I. J. Math. Phys. 25 (1–4), 279–300.
Reissner, E., 1946b. Stresses and small displacements of shallow spherical shells. II. J. Math. Phys. 25 (1–4), 80–85.
Samuelson, L.A., Eggwertz, S., 1992. Shell Stability Handbook. Elsevier Applied Science, London.
Seaman, L., 1962. The Nature of Buckling in Thin Spherical Shells (Ph.D. thesis). Massachusetts Institute of Technology, Cambridge, MA.
Sieber, J., Hutchinson, J.W., Thompson, J.M.T., 2020. Buckling thresholds for pre-loaded spherical shells subject to localized blasts. J. Appl. Mech. 87 (3).
Thompson, J.M.T., 2015. Advances in shell buckling: theory and experiments. Int. J. Bifurcation Chaos 25 (1), 1530001.
Thompson, J.M.T., Hutchinson, J.W., Sieber, J., 2017. Probing shells against buckling: a nondestructive technique for laboratory testing. Int. J. Bifurcation Chaos 27 (14), 1730048.
Thompson, J.M.T., Sieber, J., 2016. Shock-sensitivity in shell-like structures: with simulations of spherical shell buckling. Int. J. Bifurcation Chaos 26 (2), 1630003.
Timoshenko, S.P., Woinowsky-Krieger, S., 1959. Theory of Plates and Shells. McGraw-hill, New York.
Tsien, H.-S., 1942. A theory for the buckling of thin shells. J. Aeronaut. Sci. 9 (10), 373–384.
Virot, E., Kreilos, T., Schneider, T.M., Rubinstein, S.M., 2017. Stability landscape of shell buckling. Phys. Rev. Lett. 119 (22), 224101.
Yadav, K.K., Cuccia, N.L., Virot, E., Rubinstein, S.M., Gerasimidis, S., 2021. A nondestructive technique for the evaluation of thin cylindrical shells' axial buckling capacity. J. Appl. Mech. 88 (5), 051003.
Yadav, K.K., Gerasimidis, S., 2020. A nondestructive method to find the buckling capacity for thin shells. In: Proceedings of the Annual Stability Conference. Structural Stability Research Council, Atlanta, GA.
Yan, D., Pezzulla, M., Cruveiller, L., Abbasi, A., Reis, P.M., 2021. Magneto-active elastic shells with tunable buckling strength. Nature Commun. 12 (1), 2831.
Yan, D., Pezzulla, M., Reis, P.M., 2020b. Buckling of pressurized spherical shells containing a through-thickness defect. J. Mech. Phys. Solids 138, 103923.
Zoelly, R., 1915. Ueber ein Knickungsproblem an der Kugelschale (Ph.D. thesis). ETH Zürich, Zürich, Switzerland.